

Foreign Circular Element Detection in Chest X-rays for Effective Automated Pulmonary Abnormality Screening

ABSTRACT

In automated chest X-ray screening (to detect pulmonary abnormality: Tuberculosis (TB), for instance), the presence of foreign element such as buttons and medical devices hinders its performance. In this paper, using digital chest radiographs, we present a new technique to detect circular foreign element, within the lung regions. We first compute edge map by using several different edge detection algorithms, which is followed by morphological operations for potential candidate selection. These candidates are then confirmed by using circular Hough transform (CHT). In our test, we have achieved precision, recall, and F1 score of 96%, 90%, and 92%, respectively with lung segmentation. Compared to state-of-the-art work, our technique excels performance in terms of both detection accuracy and computational time.

Keywords: chest X-ray (CXR) images, edge detection, circular foreign element, circular Hough transform (CHT), Viola-Jones, lung segmentation, morphological operations.

INTRODUCTION

Lung diseases are major threats because significant numbers of people suffer from these diseases such as Tuberculosis (WHO, 2014), pneumonia, lung cancer and pulmonary edema across the world. The advent of new powerful hardware and software techniques has triggered attempts to develop computer-aided diagnostic (CAD) systems for automatic chest x-ray screening (Karargyris et al., 2016) (Santosh et al., 2016) (Schaefer-Prokop et al., 2008). However, foreign element such as buttons on the gown that the patients were wearing or coins/buttons mistakenly swallowed by patients, within the chest x-ray images hinders the performance of the automatic screening process. Fig. 1 shows a couple of such CXRs with circular foreign element (i.e., buttons) and Fig. 2 shows a closer view of all the buttons in these CXRs. The presence of such element (especially the ones located within the lung region) hinders the CAD system performance, as they are not due to any lung abnormalities and therefore should not be considered. Therefore, in the screening process precise detection of foreign element is an important issue for screening of chest diseases in CAD system. In this paper, we focus on automatically detecting foreign circular element in CXR images.

In computer vision and image analysis, circle detection has a rich state-of-the-art (Chen & Wu, 2014) (Duda & Hart, 1972) (Rad et al., 2003) (Wu et al., 2013) (Zhou & He, 2015).

Applications vary from document understanding: graphics recognition (Dosch et al., 2000) (Santosh, 2011) (Santosh et al., 2012) (Smith & Lamirov, 2017) (Smith & Lamirov, 2015) (Xu et al., 1990) to medical image analysis (Xue et al., 2015). Detecting circular foreign element in CXR images is a challenging and open research problem. However, in case of CXR images, we found (Xue et al., 2015) is only the work reported recently. In Xue et al., authors observed that CHT outperformed others but still, the technique is highly sensitive to intensity values. If there is not enough contrast between the element (buttons in CXRs) and the background image, then the

performance of CHT degrades drastically. On the other hand, Viola-Jones algorithm has high false detection rate that can degrade the performance of the CAD system.

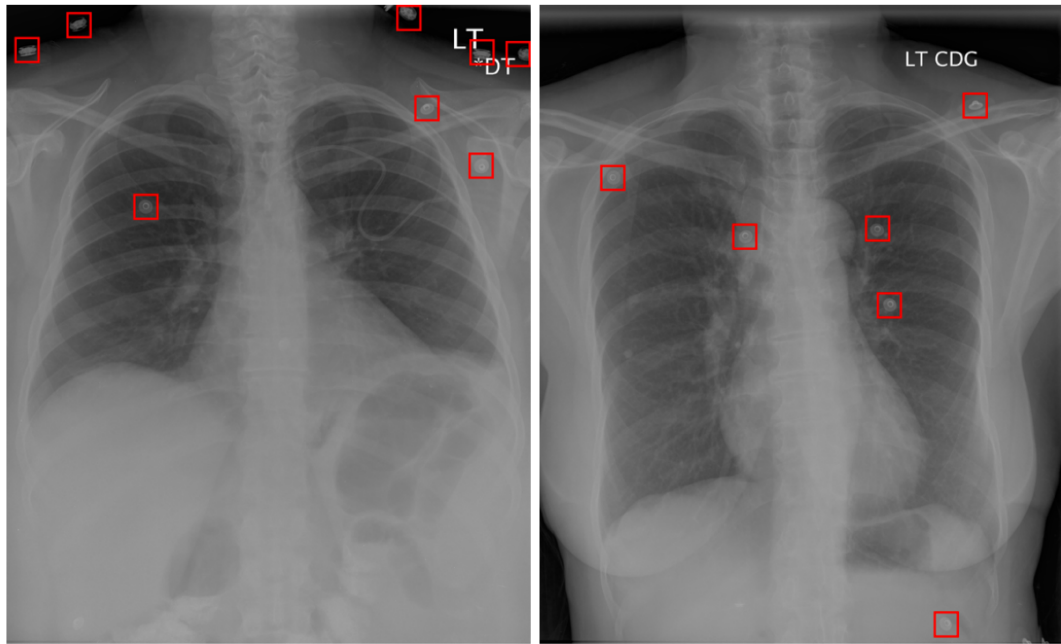


Fig. 1. CXRs containing buttons, boxes marked by red indicate the location of buttons in the images.

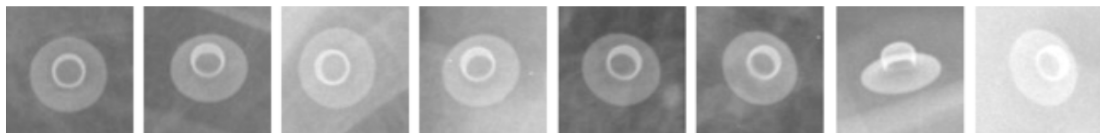


Fig. 2. Closer view of all the buttons in above chest x-ray images

Not limited to precision, faster tool is a must. In our proposed method, we applied intensity normalization and adjustment on input CXRs for image enhancement. For segmenting the circular candidate from the CXRs, we performed edge detection (Canny, Sobel, Prewitt, and Roberts) followed by some morphological operations (dilation, filling, and erosion) and then performed CHT for extracting the circular-like element. Finally, we compared our proposed method with the two benchmarking techniques that were reported in Xue et al. In our tests, the proposed method provides precision, recall, and F1 score of 96%, 90%, and 92%, respectively for a dataset, which is composed of 400 CXRs of size roughly 4.3K x 3.5K.

The rest of this paper is structured as follows. In section proposed technique, we give detailed overview of our proposed technique. At first, we briefly discuss the image enhancement (see section image enhancement) and then we provide a detailed description of the circular element detection process (see section candidate selection). Next, section experiments provide information about the data set, evaluation protocol, and results. Finally, in section conclusion, we conclude the paper.

THE PROPOSED TECHNIQUE

In our algorithm, we first enhanced the CXRs to increase the contrast between the circular element with their background, using intensity normalization and image adjustment. Next, we applied candidate selection (CS) on circular shape enhancement step to make the circular candidates more distinct and then we performed CHT for extracting circular shape element (e.g., buttons) in these images. For improving the performance, we segmented the lung area to identify the region of interest (ROI). Fig. 3 briefly presents the proposed method workflow.

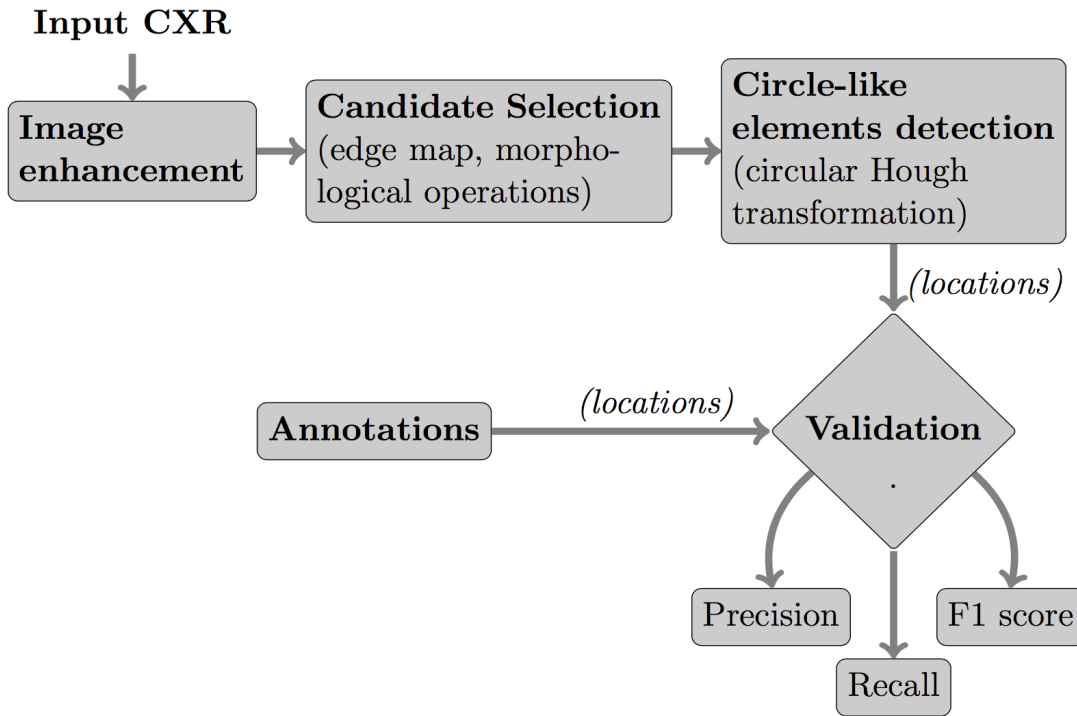


Fig. 3. It begins with image enhancement, using intensity normalization and image adjustment. After that candidate (circular element) selection is performed and finally decision is made whether the candidates are circular element.

Image enhancement:

We applied some pre-processing steps on the CXRs to improve the image quality, so that the element of interest (e.g., buttons) became more evident. The quality of the pre-processing steps strongly affects the performance of the subsequent circular element detection steps.

In our tests, we applied two pre-processing steps: intensity normalization and image adjustment. For intensity normalization, we used the same approach as in (Xue et al., 2015). For image adjustment; however, we adopted slightly different approach than (Xue et al., 2015). For images without any windowing (intensity window manually optimized by radiologists to visually enhance the lung tissue region) information, (Xue et al., 2015) performs adjustment only for low contrast images. We, however, observed that applying such adjustments always improve performance. Hence, we applied it as a common pre-processing step to all images. Fig. 4 shows one such low contrast input and the resultant image after enhancement. It also shows the histogram of pixel intensities before and after the adjustment. It can be seen from the figure that the adjusted image has more uniformly distributed intensity values and a higher contrast.

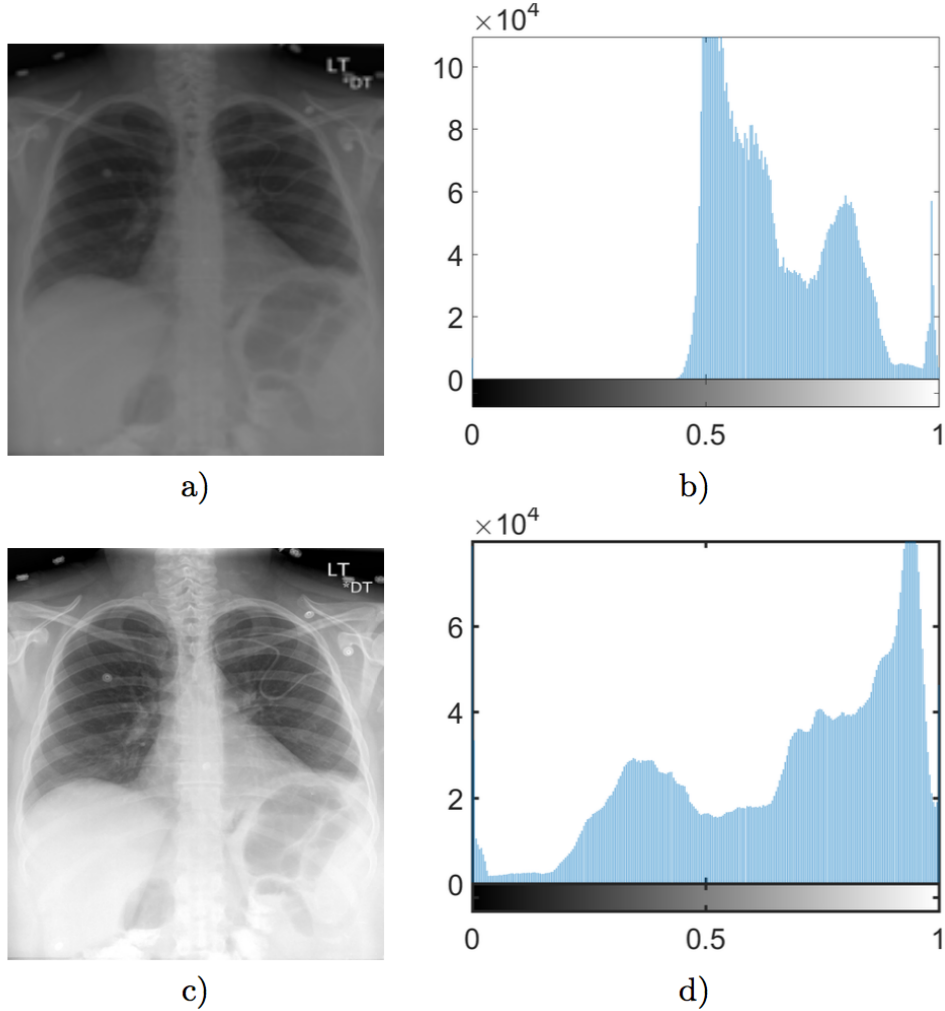


Fig. 4. Image Enhancement: a) original image, b) original image histogram, c) enhanced image, and d) enhanced image histogram.

Candidate (circular element) selection:

By analyzing the input CXRs, we observed that the buttons in the lung region are mostly of circular/elliptical shape and their boundaries are sharper than other areas. Based on these facts, we extracted circular shape element from CXRs. In our proposed technique, we applied edge detection and then performed some morphological operations on these edge-images to segment the circular candidates for candidate selection.

Edge detection. We applied edge detection to extract high gradient regions in the image. For this, we tested with four edge detection operators: Canny, Prewitt, Sobel, and Roberts. Brief explanation of those four edge detection algorithms are given below:

Canny. This edge detector (Canny, 1986) compute edges by looking for local maxima of the gradient of image. It uses derivative of a Gaussian filter for calculating the gradient. This technique uses high and low edges, considering weak edges in the output if they are connected to strong edges. It has four individual steps:

1. Smoothing: At first, blurring is applied to input image for removing the noise.
2. Finding gradients: It performs four filters for detecting horizontal, vertical and diagonal edges in the blurred image for observing the most prominent magnitudes. It gives a value for the first derivative in the horizontal direction (G_x) and the vertical direction (G_y). From this the edge gradient and direction can be determined:

$$G = \sqrt{G_x^2 + G_y^2} \quad \text{and} \quad \Theta = \text{atan2}(G_y, G_x).$$

3. Non-maximum suppression: Only local maxima should be marked as edges.
4. Double thresholding: Potential candidates are determined by applying two consecutive thresholding. Finally, hysteresis is applied for edge tracking.

Sobel. This operator (Sobel, 2014) is applied in any input gray scale image to find the approximate absolute gradient magnitude at each point. It is convoluted with original input image for calculating horizontal and vertical changes.

Prewitt. This operator (Prewitt, 1970) is similar to Sobel operator. It detects horizontal and vertical gradient components by taking difference between corresponding pixel intensities of an image. The Prewitt kernels can be decomposed as the products of an averaging and a differentiation kernel, they compute the gradient with smoothing.

Roberts. As a differential operator, Roberts cross operator (Lawrence, 1963) performs 2-D spatial gradient measurement on an input image. It has two convolution kernels where one kernel is 90° rotation of another kernel.

In Fig. 5, S1 represents the four different edge maps respectively from Prewitt, Sobel, Roberts and Canny (top to bottom) operators.

Morphological operations. Now, we applied several morphological operations (Soille, 2013) on the edge-images to segment all distinct elements in the image. The morphological operations that we performed on the edge images are given below:

Dilation. From using binary edge maps, we expected to have distinct element that can be taken as potential candidates to be circle-like. However, due to the variations in image intensity noise, the edges are discontinued. To connect those edges, we used dilation using line shaped structuring element. We used two linear structuring element S11 and S12 of length 3, oriented at angles 90° and 0°, respectively:

$$\mathbf{S11} = \begin{bmatrix} 1 \\ 1 \\ 1 \end{bmatrix}, \quad \mathbf{S12} = \begin{bmatrix} 1 & 1 & 1 \end{bmatrix}, \quad \text{and} \quad \mathbf{Sd} = \begin{bmatrix} 0 & 1 & 0 \\ 1 & 1 & 1 \\ 0 & 1 & 0 \end{bmatrix}.$$

Filling. Following connected component principle, edges are labeled. For each labeled edge, we performed a flood-fill operation that fills the holes in the element and generates element with solid interior.

Erosion. To remove noisy small element from the edge images, we eroded the image. For erosion, we used a diamond-shaped structuring element (shown above). In this step, we also suppressed structures that are connected to the image border.

In Fig. 4, steps: S1 to S4 show the step-wise outputs of morphological operations.

Decision (circle detection):

In our experiments, we used the CHT for detecting circle on candidate selection image. The brief explanation of CHT is given below:

The circular Hough transform is a specialization of Hough transform, with the purpose of finding circles in imperfect image inputs. The first step for this algorithm is to extract edges in the image. Then for each edge point (x, y) , a circle is defined in the accumulator space centered at (x, y) with a fixed radius R . The intersection point of all such circles is a maxima in the accumulator space and corresponds to the center point of the original circle that the edge points belong to. In our study, we used the size invariant circle detection method presented in (Atherton 1999). This method uses a combination of several modifications to the CHT, including the use of edge orientation, concurrent consideration of a span of circle radii, and using a compound accumulator array that has the phase corresponding to the $\log(R)$.

Our goal is to detect circular shape element in the lung region of the CXRs, since that is the main area of interest for detecting chest diseases in the CAD systems. For lung segmentation, we applied anatomical atlases with non-rigid registration algorithm (Candemir et al., 2014). Fig. 6 shows the intermediate results of circular element after candidate selection for both cases: with and without lung segmentation. For a better understanding, Fig. 7 a) shows the complete view of circular foreign element detection on candidate selection image with lung segmentation.

EXPERIMENTS

Dataset, evaluation metrics, and protocol:

In our study, we used subset of dataset maintained by National Library of Medicine, which is composed of 400 DICOM CXRs. Table 1 represents the dataset description of our experiment. We annotated corresponding ground-truths, since they are not available in this data set. For circular element detection in CXR images, we used following criteria:

- a. With lung segmentation (WSL): In WSL, we only took circular foreign element into account from the lung regions.
- b. Without lung segmentation (WoSL): In WoSL, we took all circular element across the chest X-ray images into account.

We used precision, recall, and F1 score to measure the performance.

$$Precision = \frac{TP}{TP+FP}, \quad Recall = \frac{TP}{TP+FN}, \quad \& \quad F1score = 2 \cdot \frac{Precision \cdot Recall}{Precision + Recall},$$

where TP = true positive (accurately detected buttons in the chest area), FP = false positive (inaccurately detected buttons), and FN = false negative (un-detected buttons). The following

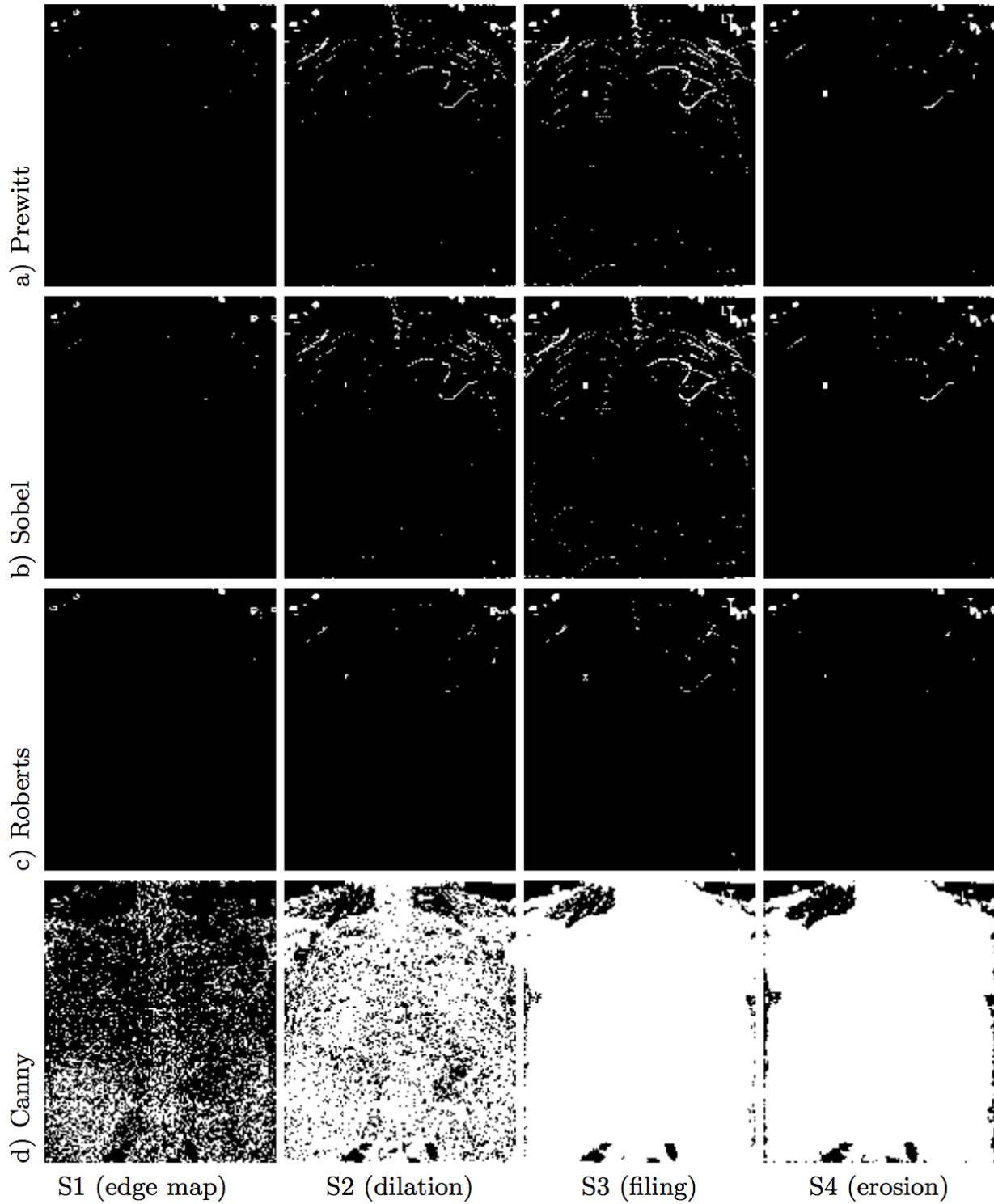


Fig. 5. Candidate selection: a), b), c), and d) show results for Prewitt, Sobel, Roberts, and Canny edge detection correspondingly. Steps S1, S2, S3, and S4 correspond to the edge detection, dilation, filling, and erosion.

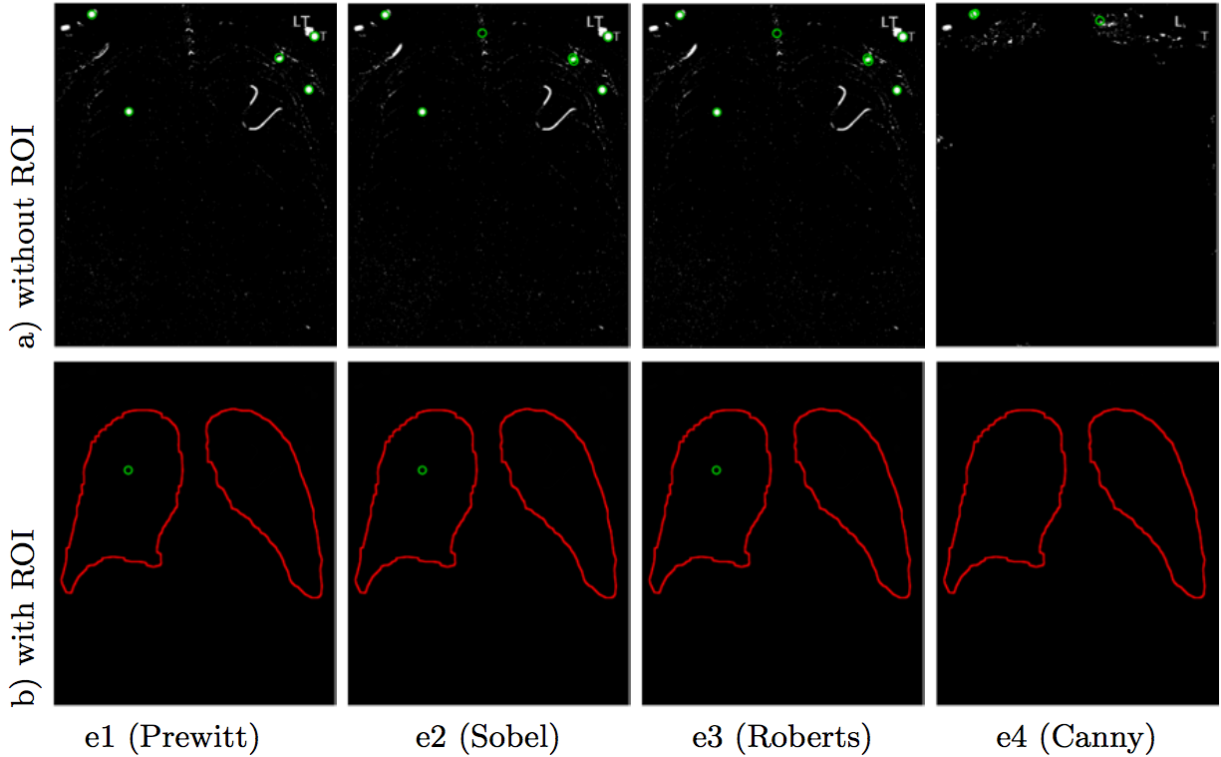


Fig. 6. Decision: e1, e2, e3, and e4 correspond to the Prewitt, Sobel, Roberts and Canny edge images followed by circular element selection steps with CHT. a) and b) show resultant circular element detection intermediate step without and with region of interest (ROI) respectively. Circles marked by green indicate the location of circular shape element on the candidate selection images.

section presents a summary of the experimental setup, test results, and comparison with the benchmarking methods.

For validating results, we performed k-fold cross validation where dataset was randomly segmented into k same size sub partitions. In that k sub partitions, k-1 sub partitions were used for training data set and one of the sub partitions was used for test dataset.

Table 1. Dataset description

# of CXRs	400
# of circular element (WLS)	325
# of circular element (WoLS)	1178

Results and analysis:

Our results. In our proposed technique, we applied four different edge operations and additional circular element enhancement step is performed on these edge images. In Fig. 5, S1-S4 show all four steps of this approach. In step S4, Prewitt edge detection performs the best with distinct circular element (less amount of outlier high gradient regions). It also is the fastest method, due to the fewer amounts of high gradient regions. Sobel operator also had similar strong circular

element but it had more outlier high gradient regions too, which leads to false detection and more computation time. On the other hand, Roberts does not have distinct circular element. However, Canny performs the worst with this approach, because Canny edge-image has many strong connected elements all over the image. Hence, after the dilation and filling steps a big portion of the image gets filled and CHT does not work well on such images. Hence, we only included results of this approach with Prewitt edge-images. The detection performance in Tables 2 and 3 with and without lung segmentation respectively. Fig. 7 a) shows circular foreign element detection results for this approach. Applying this method, we achieved 96% precision, 90% recall, and 92% F1 score using Prewitt edge image within lung segmentation.

Comparison study. We compared our result with two benchmarking techniques CHT and Viola-Jones that were used in (Xue et al., 2015) for circular element detection. For comparing our technique results with CHT and Viola-Jones, we implemented similar CHT and Viola-Jones algorithm that is used in (Xue et al., 2015). After that, we tested those algorithms with our dataset and generated the output results.

For CHT algorithm, we followed similar approach as in (Xue et al., 2015) and used the implementation in MATLAB image processing toolbox. However, instead of using a single radii range, we used a set of three radii ranges ([12, 19], [25, 45] and [46, 60]) and accumulated the results. It not only increases the speed but also accuracy of the detection process. Fig. 7 b) shows two output images of this algorithm and Tables 4 and 5, present a summary of the results with and without lung segmentation respectively.

For Viola-Jones (Viola & Jones, 2001) algorithm, we also applied similar approach as in (Xue et al., 2015). Viola-Jones is a popular element detection algorithm. It has four main steps: i) Haar feature selection, ii) integral image creation for faster computation of the Haar features, iii) training classifier, built on the AdaBoost learning algorithm, and iv) the combination of classifiers in a cascade architecture, which allows background regions to be discarded quickly. In the training stage, user provides a set of positive and negative samples of the desired element. In the testing stage, the detector scans across the image at multiple scales and locations and finds the sub-windows that contain the element. The detector also combines the overlapping multiple detections of one element into a single detection of the element. Due to data set of 400 DICOM CXRs, we trained it using 389 positive samples and 228 negative samples, and set the number of cascade stages to 15. We observed that Viola-Jones detector perform best using Haar-like feature. We used k-folding cross validation where $k = 10$ for the complete data. Table 6 represents randomly generated indices of each partition of chest X-ray images. Tables 7 and 8 provide a comparison of the results for this method using k-fold cross validation method with and without lung segmentation respectively. From the Tables 7 and 8, we can see that detection results in terms of precision has poor performance due to large number of positive training samples that leads to false detection. On the other hand, detection performance of recall is opposite. Fig. 7, c) shows two of the resultant outputs of this method. Comparisons of circular foreign element results are shown in Tables 9 and 10.

Computational time. We also measured the computational time for all circular element detection techniques. Our system has following configuration: intel core i7 processor, windows 7 operating system and MATLAB R2016a. We calculated computational time in seconds per image, on

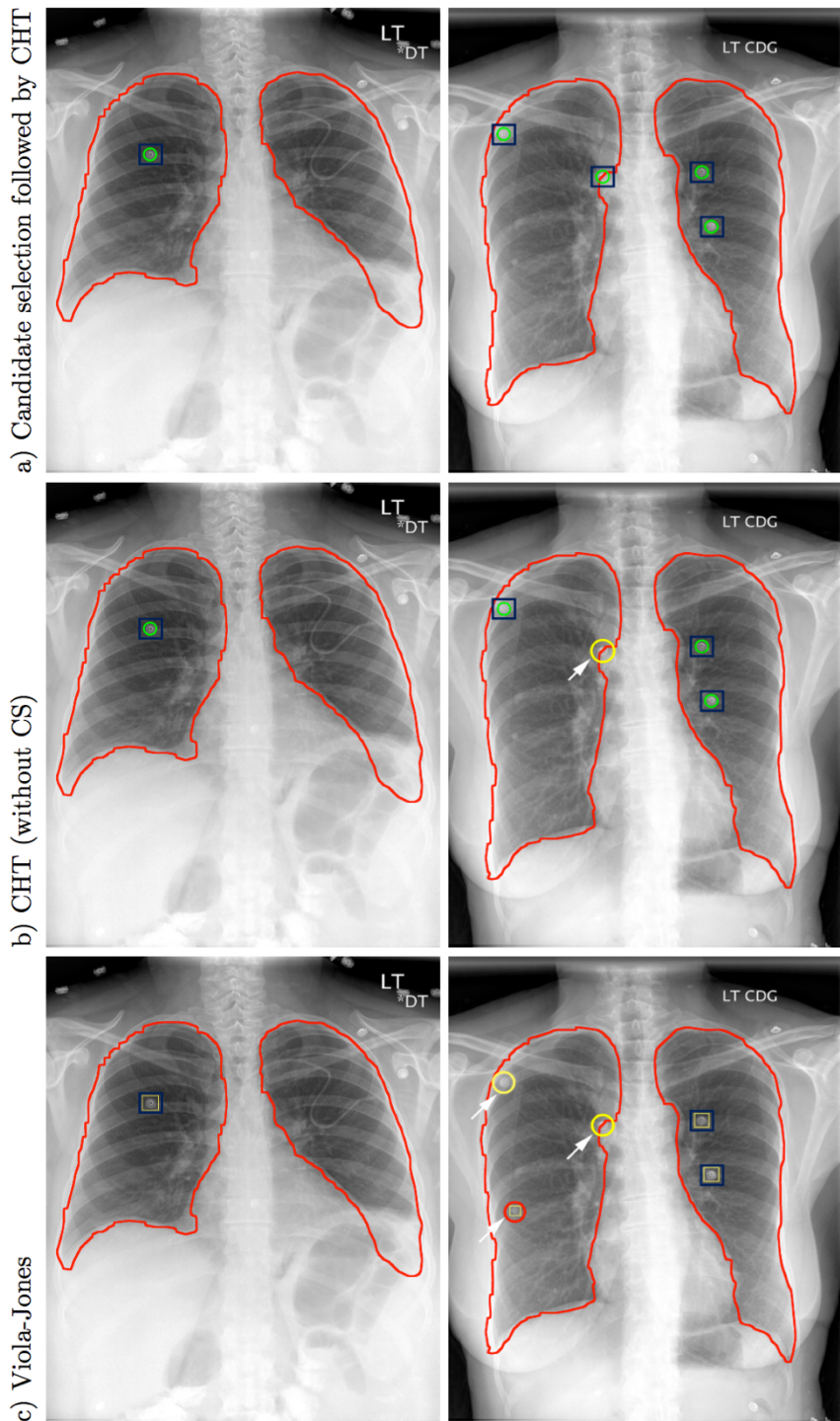


Fig. 7. Circular element detection: a), b) and c) show candidate (circular element) selection (CS) followed by CHT, CHT and Viola-Jones respectively. Here, circles marked by yellow pointed by white arrow indicate false negative, circles marked by red pointed by white arrow indicate false positive and rectangles marked by blue indicate true positive.

Table 2. Circular foreign element detection results (WLS): CHT with CS

Test	GT	Detection	TP	FP	FN	Precision	Recall	F1-score
400	325	305	293	12	32	0.96	0.90	0.92

Table 3. Circular foreign element detection results (WoLS): CHT with CS

Test	GT	Detection	TP	FP	FN	Precision	Recall	F1-score
400	1178	748	636	112	542	0.85	0.54	0.66

Table 4. Circular foreign element detection results (WLS): CHT (without CS)

Test	GT	Detection	TP	FP	FN	Precision	Recall	F1-score
400	325	256	241	15	84	0.94	0.74	0.83

Table 5. Circular foreign element detection results (WoLS): CHT (without CS)

Test	GT	Detection	TP	FP	FN	Precision	Recall	F1-score
400	1178	654	530	124	648	0.81	0.45	0.58

Table 6. k-fold cross-validation: dataset indices in each partition

Partition	Dataset indices
1	12, 243, 194, 356, 111, 172, 72, 149, 187, 318, 100, 204, 347, 247, 268, 166, 382, 373, 327, 280, 380, 5, 139, 123, 192, 388, 45, 34, 228, 357, 189, 163, 11, 370, 88, 21, 267, 263, 278, 84
2	205, 261, 17, 103, 368, 362, 295, 71, 9, 238, 19, 10, 20, 287, 335, 201, 337, 22, 148, 366, 96, 51, 53, 115, 91, 39, 23, 42, 90, 157, 257, 272, 165, 109, 203, 262, 151, 32, 349, 265
3	383, 24, 74, 33, 87, 27, 237, 202, 161, 144, 251, 184, 122, 322, 360, 256, 79, 330, 217, 182, 28, 110, 120, 43, 364, 159, 363, 252, 399, 181, 321, 333, 391, 73, 58, 218, 63, 381, 239, 271
4	38, 6, 26, 131, 25, 74, 302, 105, 314, 306, 365, 62, 215, 273, 374, 293, 233, 168, 367, 328, 56, 344, 208, 231, 142, 319, 66, 308, 353, 339, 153, 162, 248, 52, 177, 170, 147, 288, 129, 279
5	199, 276, 173, 35, 290, 116, 245, 389, 112, 160, 289, 371, 114, 260, 77, 294, 193, 207, 211, 137, 97, 317, 76, 158, 346, 232, 313, 348, 358, 304, 48, 210, 393, 186, 41, 213, 191, 230, 143, 283
6	241, 196, 133, 117, 376, 390, 174, 190, 185, 340, 101, 355, 284, 176, 132, 130, 89, 258, 60, 298, 301, 336, 315, 395, 154, 244, 134, 332, 140, 55, 343, 386, 369, 198, 234, 29, 379, 93, 286, 266
7	81, 80, 214, 259, 124, 246, 270, 7, 229, 384, 385, 15, 167, 152, 240, 250, 296, 334, 155, 375, 316, 82, 68, 83, 175, 102, 400, 300, 223, 121, 309, 54, 125, 253, 1, 352, 212, 99, 219, 85
8	195, 46, 57, 378, 242, 312, 8, 95, 30, 249, 36, 323, 291, 331, 126, 394, 303, 31, 269, 37, 67, 398, 156, 179, 118, 387, 224, 226, 351, 338, 325, 61, 222, 146, 4, 206, 178, 292, 307, 354
9	254, 285, 342, 264, 311, 281, 341, 135, 275, 227, 94, 104, 220, 180, 59, 16, 197, 188, 98, 392, 377, 106, 305, 225, 221, 236, 310, 108, 128, 150, 65, 13, 69, 70, 2, 282, 396, 119, 138, 345
10	329, 183, 3, 64, 235, 78, 86, 397, 142, 319, 66, 308, 353, 339, 153, 162, 248, 52, 177, 170, 147, 288, 129, 279, 44, 299, 107, 372, 49, 47, 361, 209, 233, 168, 367, 328, 56, 344, 208, 231

Table 7. Circular foreign element detection results (WLS): Viola-Jones

Test	Train	GT	Detection	TP	FP	FN	Precision	Recall	F1 score
1	2,3,4,5,6,7,8,9,10	28	100	28	72	0	0.28	1	0.43
2	1,3,4,5,6,7,8,9,10	34	119	34	85	0	0.28	1	0.44
3	1,2,4,5,6,7,8,9,10	28	103	28	75	0	0.27	1	0.42
4	1,2,3,5,6,7,8,9,10	37	117	37	80	0	0.31	1	0.48
5	1,2,3,4,6,7,8,9,10	45	125	45	80	0	0.36	1	0.52
6	1,2,3,4,5,7,8,9,10	53	142	53	83	0	0.37	1	0.54
7	1,2,3,4,5,6,8,9,10	52	122	52	70	0	0.42	1	0.59
8	1,2,3,4,5,6,7,9,10	41	102	41	61	0	0.40	1	0.57
9	1,2,3,4,5,6,7,8,10	55	119	55	64	0	0.46	1	0.63
10	1,2,3,4,5,6,7,8,9	48	119	48	71	0	0.40	1	0.57
Average						0.36	1	0.52	

Table 8. Circular foreign element detection results (WoLS): Viola-Jones

Test	Train	GT	Detection	TP	FP	FN	Precision	Recall	F1 score
1	2,3,4,5,6,7,8,9,10	103	294	90	204	13	0.30	0.87	0.45
2	1,3,4,5,6,7,8,9,10	117	334	109	225	8	0.32	0.93	0.48
3	1,2,4,5,6,7,8,9,10	100	284	95	189	5	0.33	0.95	0.49
4	1,2,3,5,6,7,8,9,10	108	304	104	200	4	0.34	0.96	0.50
5	1,2,3,4,6,7,8,9,10	85	288	78	210	7	0.27	0.91	0.41
6	1,2,3,4,5,7,8,9,10	144	307	137	170	7	0.44	0.95	0.60
7	1,2,3,4,5,6,8,9,10	129	315	120	195	9	0.38	0.93	0.54
8	1,2,3,4,5,6,7,9,10	118	295	115	180	3	0.38	0.97	0.55
9	1,2,3,4,5,6,7,8,10	135	290	130	160	5	0.44	0.96	0.61
10	1,2,3,4,5,6,7,8,9	138	299	129	170	9	0.43	0.93	0.59
Average						0.37	0.94	0.53	

Table 9. Comparison of circular foreign element detection results (WLS)

Method	Precision	Recall	F1 score
CS followed by CHT	0.96	0.90	0.92
Viola-Jones	0.36	1	0.52
CHT	0.94	0.74	0.83

Table 10. Comparison of circular foreign element detection results (WoLS)

Method	Precision	Recall	F1 score
CS followed by CHT	0.85	0.54	0.66
Viola-Jones	0.37	0.94	0.53
CHT	0.81	0.45	0.58

Table 11. Computational time of button detection techniques

Method	Time (in second)
CS followed by CHT	8.52
Viola-Jones	18.83
CHT	29.02

average. Average CXR size is around 4.3K x 3.5K. Table 11, shows the computational time of all circular element detection techniques. Note that in (Xue et al., 2015), authors did not report computational time.

CONCLUSION

In this work, we have focused on identifying circular foreign element such as buttons, coins appearing in lung regions of the chest X-ray images. We presented a novel technique for circular foreign element detection. Our proposed technique is encouraging, both in terms of detection accuracy and computation time. Using Prewitt edge detection followed by circular candidate selection and CHT, we achieved perfect detection of 96% precision, 90% recall, and 92% F1 score with lung segmentation. As future work, we plan to improve the detection results of the circular element across the CXRs and extend this work to detect other types of non-circular foreign element (e.g., medical tubes) that usually appears in CXRs.

ACKNOWLEDGEMENTS

We are grateful to the US National Library of Medicine for giving us opportunity to access their dataset for our study. We also thank to Dr. Sameer Antani (Staff Scientist, US National Library of Medicine, NIH), for his guidance during the visit at the USD on 10/17/2016.

REFERENCES

- Xue, Z., Candemir, S., Antani, S., Long, L. R., Jaeger, S., Demner-Fushman, D., & Thoma, G. R. (2015). Foreign element detection in chest X-rays: Bioinformatics and Biomedicine (BIBM), 2015 IEEE International Conference on (pp. 956-961), IEEE.
- Atherton, T. J., & Kerbyson. D. J. (1999), Size invariant circle detection, *Image and Vision computing* (vol. 17, num. 11, pp. 795-803), Elsevier.
- Viola, P., & Jones, M. (2001). Rapid element detection using a boosted cascade of simple features. *Computer Vision and Pattern Recognition, 2001. CVPR 2001. Proceedings of the 2001 IEEE Computer Society Conference on*(vol. 1, pp. I-511), IEEE.
- Candemir, S., Jaeger, S., Palaniappan K., Musco, J. P., Singh, R. K., Xue, Z., Karargyris, A., Antani, S., Thoma, G., McDonald, C. J. (2014). Lung segmentation in chest radiographs using anatomical atlases with nonrigid registration, *Medical Imaging, IEEE Transactions on* (vol. 33, num. 2, pp. 577-590), IEEE.
- Canny, J. (1986). A computational approach to edge detection, *Pattern Analysis and Machine Intelligence, IEEE Transactions on* (num. 6, pp. 679—698), IEEE.

Prewitt, J. MS. (1970). Element enhancement and extraction, Picture processing and Psychopictorics (vol.10, num. 1, pp. 15-19), Academic Press, New York.

Sobel, I. (2014). History and definition of the sobel operator, Retrieved from the World Wide Web.

Lawrence, G. R. (1963). Machine perception of three-dimensional solids, Ph. D. Thesis, Massachusetts Institute of Technology Cambridge, MA, USA.

Soille, P. (2013). Morphological image analysis: principles and application, Springer Science & Business Media.

Schaefer-Prokop, C., Neitzel, U., Venema, H. W., Uffmann, & M., P., Mathias. (2008). Digital chest radiography: an update on modern technology, dose containment and control of image quality, European radiology (vol.18, num. 9, pp. 1818—1830), Springer.

World Health Organization (WHO) (2014): global tuberculosis report.

Santosh, K. C., Vajda, S., Antani, S., & Thoma, G. R., (2016). Edge map analysis in chest X-rays for automatic pulmonary abnormality screening, International Journal of Computer Assisted Radiology and Surgery, pp. 1-10, issn. 1861-6429.

Karargyris, A., Siegelman, J., Tzortzis, D., Jaeger, S., Candemir, S., Xue, Z., Santosh, KC., Vajda, S., Antani, S., Folio, L., & others (2016). Combination of texture and shape features to detect pulmonary abnormalities in digital chest X-rays, International journal of computer assisted radiology and surgery, vol.11, num.1, pp. 99--106, Springer.

Smith, E. H. B., & Lamiroy, B. (2015). Circle Detection Performance Evaluation Revisited, International Workshop on Graphics Recognition, pp. 3--18, Springer.

Santosh, KC., Lamiroy, B., & Wendling, L. (2012). Symbol recognition using spatial relations, Pattern Recognition Letters, vol.33, num.3, pp.331—341, Elsevier.

Wu, J., Chen, K., & Gao, X.,(2013), Fast and accurate circle detection using gradient-direction-based segmentation, JOSA A, vol.30, num.6, pp.1184--1192, Optical Society of America.

Duda, R. O., & Hart, P. E.,(1972). Use of the Hough transformation to detect lines and curves in pictures, Communications of the ACM, vol.15, num.1, pp.11--15, ACM.

Xu, L., Oja, E., & Kultanen, P.,(1990). A new curve detection method: randomized Hough transform (RHT), Pattern recognition letters, vol.11, num.5, pp.331—338, Elsevier.

Rad, A. A., Faez, K., & Qaragozlou, N., (2003). Fast Circle Detection Using Gradient Pair Vectors, Dicta, pp.879—888.

Chen, K., & Wu, J., (2014). One-dimensional voting scheme for circle and arc detection, JOSA A, vol.31, num.12, pp.2593--2602, Optical Society of America.

Santosh, KC., (2011). Graphics recognition using spatial relations and shape analysis, Universite de Lorraine.

Zhou, B., & He, Yang, (2016). Fast Circle Detection Using Spatial Decomposition of Hough Transform, International Journal of Pattern Recognition and Artificial Intelligence, pp.1755006, World Scientific.

Dosch, P. T., Karl, A.h-Soon, & Christian and Masini, G. (2000). A complete system for the analysis of architectural drawings, International Journal on Document Analysis and Recognition, vol.3, num.2, pp.102--116, Springer.

Barney, S. E. H., & Lamiray, B. (2017). Circle Detection Performance Evaluation Revisited. In: Lamiray B., Dueire Lins R. (eds) Graphic Recognition. Current Trends and Challenges. GREC 2015. Lecture Notes in Computer Science, vol. 9657, Springer, Cham.